ARTICLES
https://doi.org/10.1038/s41551-021-00710-3

nature biomedical engineering

Computational modelling of perivascular-niche dynamics for the optimization of treatment schedules for glioblastoma

Amanda Randles[1], Hans-Georg Wirsching[2,3], Jamie A. Dean[4,5,6], Yu-Kang Cheng[4], Samuel Emerson[7], Siobhan S. Pattwell[2], Eric C. Holland[2] ✉ and Franziska Michor[4,5,6,8,9,10] ✉

Glioblastoma stem-like cells dynamically transition between a chemoradiation-resistant state and a chemoradiation-sensitive state. However, physical barriers in the tumour microenvironment restrict the delivery of chemotherapy to tumour compartments that are distant from blood vessels. Here, we show that a massively parallel computational model of the spatiotemporal dynamics of the perivascular niche that incorporates glioblastoma stem-like cells and differentiated tumour cells as well as relevant tissue-level phenomena can be used to optimize the administration schedules of concurrent radiation and temozolomide—the standard-of-care treatment for glioblastoma. In mice with platelet-derived growth factor (PDGF)-driven glioblastoma, the model-optimized treatment schedule increased the survival of the animals. For standard radiation fractionation in patients, the model predicts that chemotherapy may be optimally administered about one hour before radiation treatment. Computational models of the spatiotemporal dynamics of the tumour microenvironment could be used to predict tumour responses to a broader range of treatments and to optimize treatment regimens.

Glioblastoma (GBM) is a devastating disease. Despite multimodal treatment comprising surgery, radiotherapy and alkylating chemotherapy with temozolomide (TMZ)—which is the current standard of care for all patients after diagnosis[1]—the prognosis of GBM is invariably fatal, with a median overall survival of about 1 year[2,3]. Clinical trials evaluating multiple different dose-escalation approaches on the basis of the linear quadratic model of classical radiobiology have failed to increase survival[4]. Treatment strategies informed by an alternative approach explicitly modelling the mechanisms of treatment resistance and intratumor heterogeneity are necessary to achieve improved outcomes for patients.

Histologically, GBMs are characterized by extensive proliferation of disrupted microvessels[5], which create a distinct microenvironment that is designated the perivascular niche (PVN)[6]. This PVN is defined by the spatial relationship between cancer cells and endothelial cells[6]. Chemoradiation-resistant GBM stem-like cells (GSCs) preferentially reside in this PVN[6], and localized signalling from the tumour microenvironment maintains and induces the stem-like phenotype of GSCs through nitric oxide or notch ligands[7,8]. Although other cell types may contribute to these functional properties of the PVN, endothelial cells have been identified as the key mediators of stemness[6,7,9]. GBM cells dynamically transition between a more stem-like chemoradiation-resistant state and a more differentiated chemoradiation-sensitive state. Dedifferentiation of more differentiated cells to more stem-like cells occurs within hours after administration of radiation[8]. Accounting for this spatially explicit heterogeneity remains a challenge, with direct implications on the clinical management of this disease, as physical barriers in the tumour microenvironment restrict chemotherapy delivery to tumour compartments that are distant from the blood vessels.

In this Article, we hypothesize that the use of a computational model that quantifies how the spatial location of cells influences their sensitivity to therapy could be used to identify an optimized schedule for the administration of therapy for GBM that would maximize survival. To test this hypothesis, we developed a massively parallel, multiscale computational model of PVN dynamics that links phenomena that occur at the cellular and tissue levels. On the basis of the parameter values measured in mouse models of GBM, we identified a chemoradiation administration schedule that is predicted to optimize treatment efficacy. We validated our computational model predictions in a mouse PDGF-driven GBM model, which shows that the optimized schedule indeed increased survival. This method identified a schedule that could be difficult to implement in the clinic due to the requirement to administer radiotherapy at specific times and multiple times a day. However, it elucidated the finding that a key driver in determining optimal scheduling was the time between the administration of chemotherapy and radiotherapy. We next used our computational model to predict an optimal time for a single dose of each, administering TMZ 41 min before radiation given in standard fractionation, and showed in a mouse model that optimizing timing between therapies improved survival. Using human pharmacokinetics parameters, we

[1]Department of Biomedical Engineering, Duke University, Durham, NC, USA. [2]Division of Human Biology, Fred Hutchinson Cancer Research Center, Seattle, WA, USA. [3]Department of Neurology, University Hospital and University of Zurich, Zurich, Switzerland. [4]Department of Data Science, Dana-Farber Cancer Institute, Boston, MA, USA. [5]Department of Biostatistics, Harvard T. H. Chan School of Public Health, Boston, MA, USA. [6]Department of Stem Cell and Regenerative Biology, Harvard University, Cambridge, MA, USA. [7]Department of Neurological Surgery, University of Washington, Seattle, WA, USA. [8]Center for Cancer Evolution, Dana-Farber Cancer Institute, Boston, MA, USA. [9]The Broad Institute of MIT and Harvard, Cambridge, MA, USA. [10]The Ludwig Center, Harvard University, Boston, MA, USA. ✉e-mail: eholland@fredhutch.org; michor@jimmy.harvard.edu

found an optimum time difference of 57 min between TMZ and radiation. Our findings lay the conceptual foundation for improved approaches for the clinical management of this disease.

Results

The aim of this research is to test the hypothesis that a computational model quantifying the effects of spatial location of cells on sensitivity to therapy can identify an optimized schedule for therapeutic administration for GBM that maximizes survival. To this end, we developed a spatially explicit, agent-based model to capture responses to different therapeutic regimens. We used the model to identify non-standard radiation-treatment (RT) schedules that are predicted to lead to optimal and suboptimal outcomes as measured by fractional volume changes of the tumour. Fractional volume change is defined as the percentage change in the overall volume of the tumour. Efficacy was tested through the use of a mouse GBM model. On the basis of this initial study, the optimal offset between radiotherapy and chemotherapy, using standard fractionation, was determined and validated in the mouse model as compared to current standard of care.

Development of a massively parallel computational model of GBM treatment response. We developed a spatially explicit stochastic modelling approach to investigate the dynamics of GSCs and differentiated GBM cells within the PVN (Fig. 1a). In our framework, the PVN is modelled as a collection of autonomous decision-making agents that act independently in accordance to their individual environment and rules. We considered the PVN to be a cylindrical region in the brain and investigated two-dimensional (2D) cross-sections of the region for individual simulations. Our framework contains four cell types: endothelial cells, microenvironmental (stromal) cells, GSCs and differentiated tumour cells (DTCs). The former two cell types are created at the initiation of the simulation and do not undergo division or death, but instead define the spatial structure of the PVN. Vascular remodelling after chemoradiation was not simulated because it typically occurs in the range of weeks after irradiation[10] and is therefore beyond the time scale of our theoretical and experimental approach, whereas early post-irradiation endothelial cell apoptosis occurs only after single-dose suprathrapeutic irradiation[11] and radiation-induced recruitment of bone marrow-derived cells does not contribute to vasculogenesis, but rather supports endothelial cell survival[10]. By contrast, GSCs divide asymmetrically to produce DTCs that then divide symmetrically z times before terminally differentiating or dying. Furthermore, the model incorporates the possibility of differentiation, dedifferentiation and cellular quiescence/arrest effects on cells that may depend on therapy or paracrine signals. Further details of the model design, parameter estimation, and implementation of radiation and chemotherapy effects are provided in the Methods. Supplementary Table 1 displays a list of parameters and their definitions as well as values estimated from GBM mouse models, whereas Fig. 1a shows a schematic representation of the chemoradiation model. Figure 1b shows the overall workflow of the project. An instantiation of the stochastic model for tumour growth is shown in Fig. 2a. Our approach was implemented as a massively parallel simulation framework and computation for the mouse schedules was completed using the Vulcan supercomputer, an IBM Blue Gene/Q system, at the Lawrence Livermore National Laboratory. To complete the necessary simulations, 36 million central processing unit (CPU) hours (4,109 years) on 131,072 cores were used. For the human studies, 500,000 CPU hours were used on the Duke Compute Cluster and 2 million CPU hours were used on the Quartz supercomputer at the Lawrence Livermore National Laboratory.

Optimizing the chemoradiotherapy administration schedule. The massively parallel model, together with simulated annealing, was used to derive an optimized radiation schedule in the presence of TMZ (Methods). Parameters were selected that captured the treatment response in the PDGF-driven mouse model (Methods). We investigated 5 d of treatment with a total of 10 Gy radiation, with follow-up until death. The administration of TMZ was fixed to occur every day (Monday to Friday) at 15:00. To determine an improved schedule, the time and fractionation of radiation was varied. Radiotherapy could be administered Monday to Friday between 08:00 and 17:00, on the hour. Even though the computational model was parameterized using mouse data and validated in a mouse study, constraints were derived from information of the Brigham and Women's Hospital/Dana-Farber Cancer Institute radiation oncology clinic for potential clinical translation in the future. The constraints specify that there could be no more than 8 h between the first and last dose per day, the maximum dose at one time was 3 Gy and the maximum total dose per day was 4 Gy. There could be no more than three treatments per day and the maximum total dose over the course of treatment was set to 10 Gy.

Using this approach, we predicted the maximal survival time and investigated the treatment response (Fig. 2b,c) under our identified, optimized radiation administration schedule, as well as a control sequence that was predicted to perform worse and a zero-offset schedule that was designed to mimic the standard-of-care treatment in patients (Table 1a). When performing the parallel stochastic optimization routine, we compared the fitness (that is, the total number of tumour cells present 30 d after treatment conclusion compared with that of the initialization condition) of a range of schedules (1,024 in each generation) over 30 generations. In this case, generation refers to the step or round of the simulated annealing heuristic. On average, when calculated for 128 instantiations of the stochastic simulation, we found that the predicted optimum schedule indeed resulted in a slower expansion of DTCs compared with the suboptimum and zero-offset schedules (Fig. 3a). As the suboptimum and zero-offset schedules had similar predicted outcomes, we focused on the comparison between optimum and suboptimum schedules in the following analyses. The differences in expansion as defined by the increase in fractional volume are significantly different between optimum and suboptimum schedules, with a mean fractional volume change of 3.67 for the optimal schedule and 4.72 for the suboptimal schedule ($P<0.0001$, two-tailed t-test). The observed variation was due to the stochasticity of the simulations and not due to uncertainties in the parameter values. We next performed sensitivity analysis to obtain information on the relative effects that changes in the parameter values have on outcome.

Computational model sensitivity. We conducted sensitivity studies to identify which parameters had the strongest influence on the results (Fig. 3b and Supplementary Fig. 1). Throughout these studies, the parameters of our model were systematically changed and the effect on fractional volume change was measured. This approach was taken to address questions relating to different individuals reacting to the drug differently but, more importantly, it was used to derive an understanding of which parameters were influencing the outcome and why. We completed a series of uncertainty quantification tests to determine the effect of varying parameters such as the radius of the blood vessel, the maximum number of cell divisions before apoptosis and the cut-off for the number of times a cell divides before terminally differentiating. The radius of the blood vessel demonstrated no significant impact on the results when the size was varied between 1.5 µm and 3 µm (Supplementary Fig. 1a), which is on par with the size of vessels found in this region[12,13]. However, as the vessel radius increased beyond 3.5 µm, a significant change in relative fitness was observed. This observation was probably due to the influence of the diffusion of TMZ from the vessel wall being less substantial in larger vessels, reducing the role that the chemotherapy component of the schedule has in determining cell

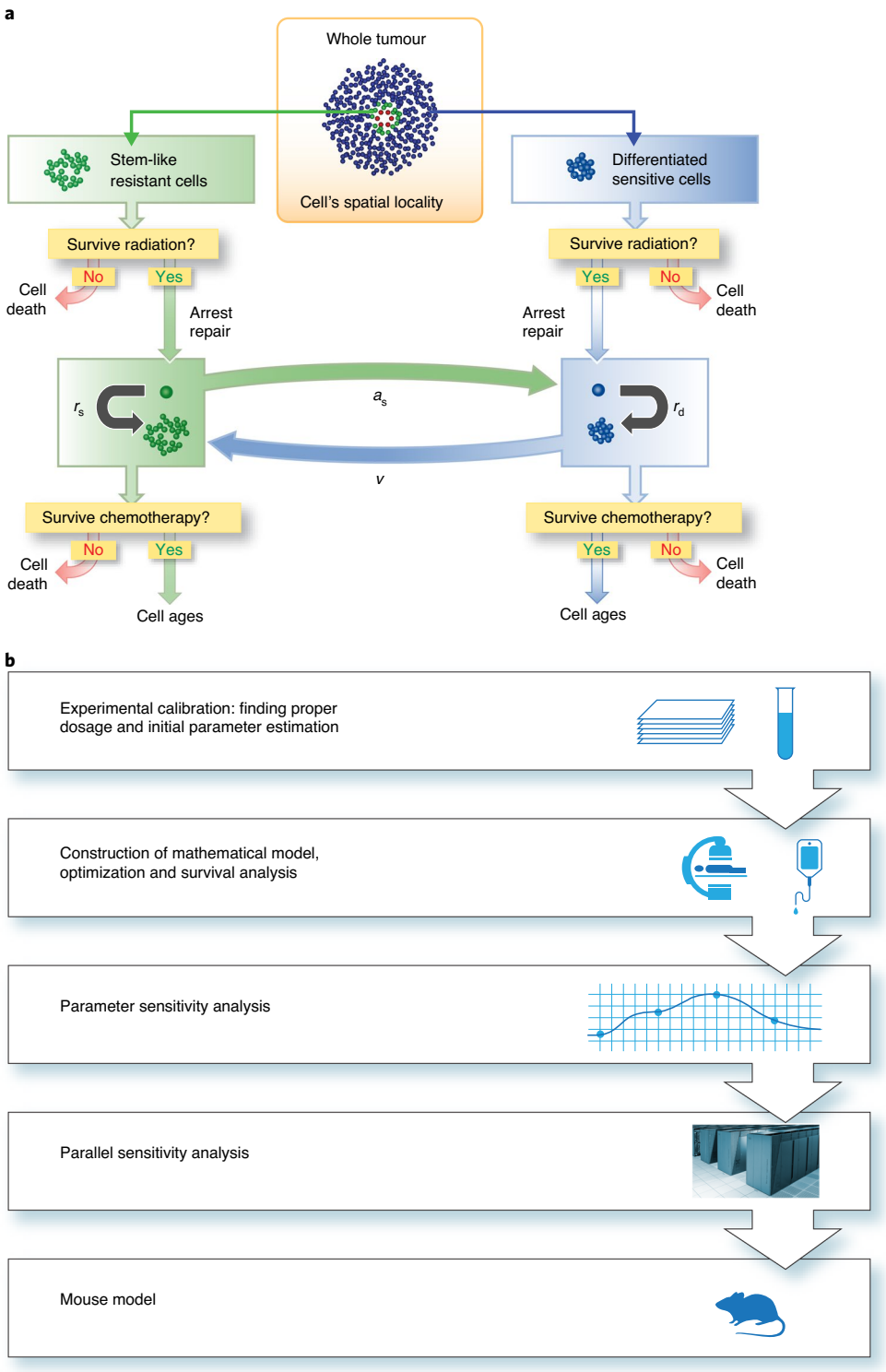

Fig. 1 | A computational model of the GBM microenvironment. a, Schematic of the computational modelling approach used to describe the chemoradiation response. r_d is the proliferation rate of differentiated sensitive cells after exiting quiescence, r_s is the proliferation rate of stem-like resistant cells after exiting quiescence, a_s is the rate at which stem-like resistant cells convert to differentiated sensitive cells and v is the rate of reversion of differentiated sensitive cells to stem-like resistant cells. **b**, Summary of the workflow.

behaviour at the centre of large vessels. As the vessels in the mouse and human PVN have a radius of less than 3.5 µm, we concluded that a change in vessel size has no significant effect on the results. We also found that varying the number of times a DTC could divide before terminally dedifferentiating (z) and the cut-off for the number of times a cell could dedifferentiate (z_{revert}) led to no significant difference being observed (Supplementary Fig. 1b,c).

We also modelled the pharmacokinetic and pharmacodynamic parameters of TMZ at relevant tissue concentrations[14] to identify whether variability in these factors could influence our findings.

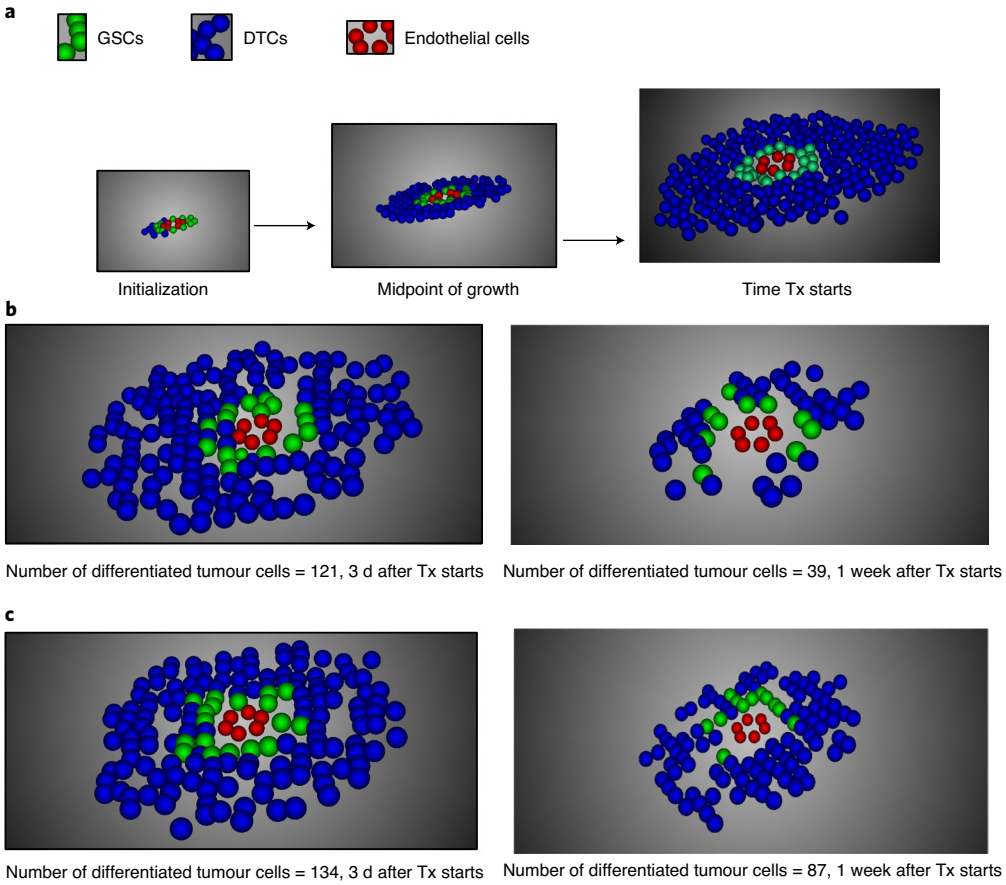

Fig. 2 | Modelling GBM growth and treatment response. a, The results of one stochastic simulation of tumour growth for three time points. Our spatially explicit stochastic process model of the PVN considers several distinct cell types, including endothelial cells (red), GSCs adjacent to the blood vessel (green) and DTCs (blue). **b**, The results of one stochastic simulation of the treatment response to chemoradiation administered according to the optimal schedule (Fig. 3a) for two time points: 3 d and 7 d after the start of treatment. **c**, The results of one stochastic simulation of the treatment response to chemoradiation administered according to the suboptimal schedule (Fig. 3a) for two time points: 3 d and 7 d after the start of treatment.

These sensitivity studies (Fig. 3b and Supplementary Fig. 1d–f) showed no significant impact ($P < 0.0001$, standard t-test) when the maximum concentration that the drug achieves, C_{max}, or the time of the maximum concentration, T_{max}, were varied by ±30%. This range was selected to capture fluctuations derived from how the drug is processed in the body. Notably, these findings are consistent with the clinical lack of benefit from dose-intensified versus standard dose TMZ regimens in patients with GBM[15,16]. The concentration at which the response is reduced by half, IC_{50}, demonstrated a small effect on the relative efficacy of the chemoradiation schedule, while the half-life of the drug, $t_{1/2}$, showed a strong effect. The efficacy of the schedule—as defined by fractional volume change 30 d from the time of treatment start—was also sensitive to the radius of the vessel at sizes above 3 µm. We found that the efficacy of the schedule was most sensitive to the drug's half-life; if the drug takes longer to clear, it is able to diffuse further and therefore not only influences cells over a longer time period but also over a larger volume[17]. This information could have an important role in developing chemotherapeutics in the future.

The improvement in terms of fitness is shown in Fig. 3c. The relative volume fraction specifying fitness is defined as the ratio of the fractional volume change at 30 d after treatment for the schedule tested in that generation to the fractional volume change at 30 d for the schedule initializing the stochastic optimization routine. The resulting number of DTCs after treatment was typically smaller with each improved schedule. The schedule continued to be optimized until the same schedule was converged on for over three generations. At this point, a local minimum was identified. To calculate the fitness of each schedule, a computationally expensive, parallel simulation was completed for 128 instances of each schedule. The breakdown of time spent in each computational function is shown in Fig. 3d.

Investigating radiation and TMZ combination schedules. Next, we used our modelling approach to simulate five previously investigated schedules[18]. We found that, in the presence of TMZ, the standard dose of 2 Gy administered each day was predicted to be the optimal of these five schedules. Due to this observation, the standard schedule was used as the template schedule to seed the parallel simulated annealing simulation for identifying the global optimum of chemoradiation administration. We set the fitness function endpoint as the number of tumour cells present 30 d after treatment initiation. Mathematically determining the global optimal schedule was not computationally tractable due to the complex interdependencies of our model. We therefore used the parallel simulated annealing model to identify an optimized combined therapeutic schedule as well as a suboptimal and zero-offset schedule (Table 1). Figure 3a shows the outcome of these schedules in terms of the number of DTCs, whereas Fig. 2 shows examples of the spatial distribution of the different cell types at different time points for both the optimized and suboptimal schedules. Qualitatively, Fig. 2 shows that the optimized schedule has fewer DTCs after treatment and the

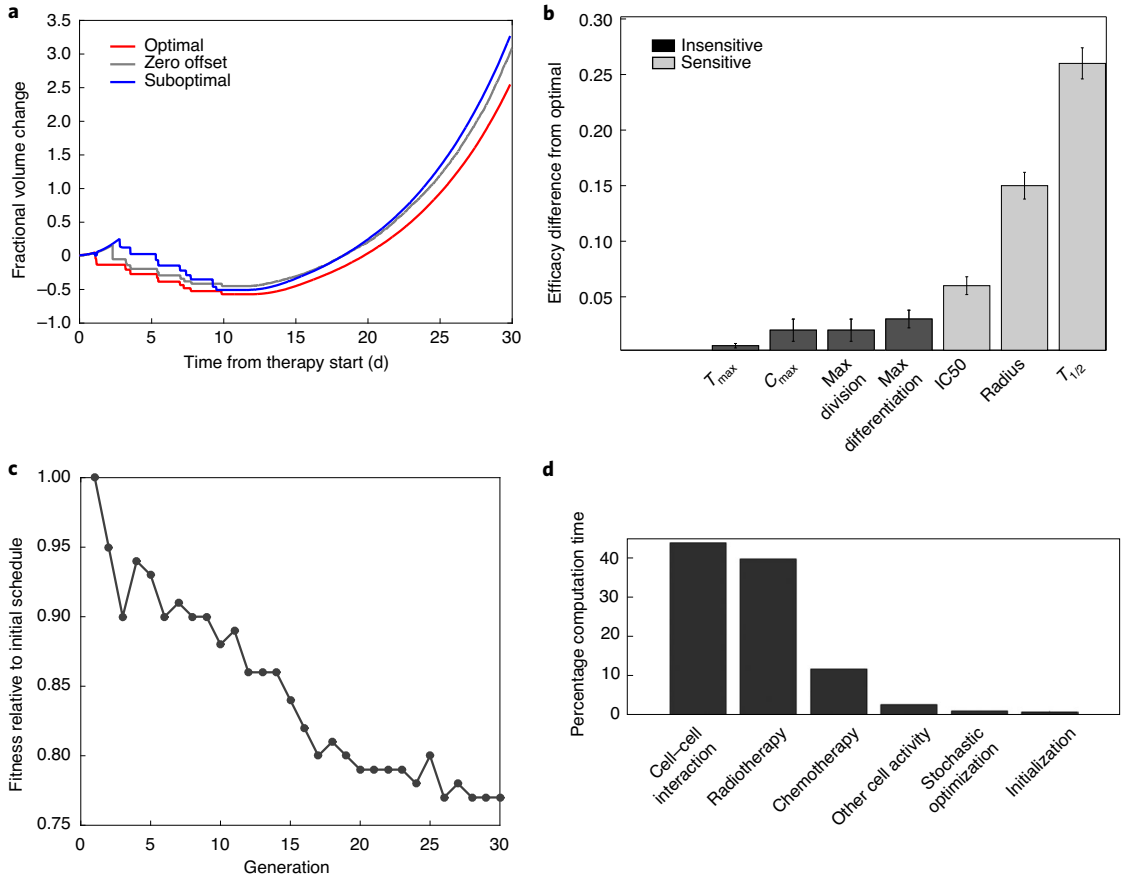

Fig. 3 | Prediction of the responses to different chemoradiation administration schedules. a, Prediction plots of the expected fractional volume change over time for the optimized versus suboptimal and zero-offset treatment schedules from Table 1. To account for stochasticity, the simulations were run 128 times to create the technical replicates required to account for stochasticity of the model. The differences in expansion as defined by increase in fractional volume are significantly different with a mean fractional volume change of 3.67 for the optimal schedule and 4.72 for the suboptimal schedule ($P < 0.0001$, two-tailed *t*-test). **b**, Sensitivity analysis of the model's parameters, ranked from least to most sensitive, as determined by the sensitivity analysis in Supplementary Fig. 1. The variables that demonstrated a significant impact when varied by ±30% are shown in light grey ($P < 0.0001$, two-tailed *t*-test), whereas those with no significant impact are shown in black ($P < 0.0001$, two-tailed *t*-test). **c**, The relative fitness across stochastic optimization generations. Each generation consisted of 1,024 different schedules being tested with 128 instances of each schedule. These instances provided the technical replicates required to account for stochasticity of the model. **d**, The percentage of time spent in each component of the 36 million CPU hours on the IBM Blue Gene/Q supercomputer.

influence of chemotherapeutic diffusion from the vessel can be seen in the distribution of the remaining cells. These observations are further confirmed quantitatively in Figs. 3a and 4. The tumour volume is significantly smaller after the optimized schedule compared with the tumour volume after the suboptimal schedule (mean difference = 0.72 mm^3, 95% CI = 0.683–0.756, $P < 0.0001$; Fig. 3a) and the distance from the vessel of GSCs versus DTCs under each schedule is significantly greater (for optimal, mean difference = 81.85 µm, 95% CI = 81.511–82.198, $P < 0.0001$; for suboptimal, mean difference = 25.7 µm, 95% CI = 25.258–26.304, $P < 0.0001$; Fig. 4a,b). The optimized versus suboptimal schedule affected the distance from the vessel centre at which the DTCs were found (mean difference = 61 µm, 95% CI = 60.13–61.87, $P < 0.0001$), as well as the location of the GSCs (mean difference = 0.07 mm, 95% CI = 0.092–0.047, $P < 0.0001$).

We next undertook a series of tests to investigate the cellular response 30 d after initiation of treatment. For this time duration from the start of the therapy to 30 d after treatment initiation, we determined the average age of GSCs (Fig. 4c) and DTCs (Fig. 4d), finding that GSCs were significantly older than DTCs (mean difference = 0.993 d, 95% CI = 0.795–1.191, $P < 0.0001$), whereas the age of GSCs had more variance. These findings primarily arose due to the proximate location of the GSCs near to the vessel wall, and these cells thereby experienced a greater effect of TMZ. Figure 4a,b shows the average distance from the vessel for both the GSCs and DTCs, demonstrating that GSCs tended to be much closer to the vessel over the course of treatment, for example, at 1 d after the start of therapy (mean difference = 22.9 mm, 95% CI = 20.99–24.93, $P < 0.0001$) and 7 d after the start of therapy (mean difference = 25.96 mm, 95% CI = 23.99–27.93, $P < 0.0001$). This localization pattern led to a fluctuation in distance as many of the cells present 1 d after treatment initiation were killed by therapy. The suboptimal schedule resulted in more DTCs on average being located further from the vessel at 1 d compared with at 7 d after treatment initiation (mean difference = 0.025 µm, 95% CI = 0.003–0.047, $P < 0.001$), an observation that is probably due to the higher concentration of the chemotherapeutic near the vessel and the associated relative increase in the chemotherapy response. The maximum distance that all cells move away from the vessel is shown in Fig. 4e, demonstrating that DTCs dictated the size of the cell population. The average cell distance from the vessel centre was greater as treatment progressed under both the optimal (mean difference = −3.25 µm,

Table 1 | Treatment arms

Group	Therapy schedule	Day 1	Day 2	Day 3	Day 4	Day 5
Mouse schedule, TMZ 50 mg kg^{-1}	Clinical RT SoC	2 Gy, 15:00	2 Gy, 15:00	2 Gy, 15:00	2 Gy, 15:00	2 Gy, 15:00
	Optimal RT fractionation	No RT	1 Gy, 09:00; 1 Gy, 16:00	1 Gy, 08:00; 2 Gy, 09:00	1 Gy, 09:00; 2 Gy, 16:00	1 Gy, 09:00; 1 Gy, 17:00
	Suboptimal RT fractionation	2 Gy; 13:00	1 Gy, 13:00; 1 Gy, 17:00	1 Gy, 14:00; 1 Gy, 15:00	2 Gy, 08:00; 1 Gy, 11:00	1 Gy, 17:00
	All RT schedules	TMZ, 15:00	TMZ, 15:00	TMZ, 15:00	TMZ, 15:00	TMZ, 15:00
Human schedule, TMZ 75 mg m^{-2}	Clinical RT SoC	2 Gy, 15:00	2 Gy, 15:00	2 Gy, 15:00	2 Gy, 15:00	2 Gy, 15:00
	Optimal offset (57 min)	TMZ, 14:03	TMZ, 14:03	TMZ, 14:03	TMZ, 14:03	TMZ, 14:03
	Zero offset	TMZ, 15:00	TMZ, 15:00	TMZ, 15:00	TMZ, 15:00	TMZ, 15:00
	Bedtime chemotherapy	TMZ, 21:00	TMZ, 21:00	TMZ, 21:00	TMZ, 21:00	TMZ, 21:00

The treatment arms used to predict responses to different chemoradiation schedules in both mice and humans. For the mouse schedules, the TMZ dosage was 50 mg kg^{-1}; for the human schedules, a dose of 75 mg m^{-2} was used. For the mouse studies, three schedules were defined. The clinical RT standard of care (SoC) reflects the current standard of care, delivering 2 Gy at 15:00. Our computational model identifies an optimal RT fractionation and suboptimal RT fractionation schedule on the basis of simulated fractional volume change. For the human studies, computational models were used to determine the optimal offset or time between administration of TMZ and radiation. Four schedules were used: (1) clinical RT standard of care; (2) the derived optimal offset; (3) zero offset, whereby radiation and TMZ were administered concurrently; and (4) when TMZ was administered at bedtime or 21:00.

95% CI = −3.35–3.14, $P < 0.0001$) and suboptimal schedules (mean difference = −6 µm, 95% CI = −6.1 to −5.9, $P < 0.0001$). However, the GSCs moved further earlier on under the optimal schedule. The change was small (0.81 µm to 0.58 µm) and, again, due to the spatial effects of the cell interaction with the chemotherapeutic. The composition of the cell population is shown in Fig. 4f, visualizing the percentage of GSCs at each daily time point. In all cases, GSCs made up less than 2% of the population. Under the optimal treatment schedule, this was further reduced from 0.82% to 0.486%; by contrast, under the control schedule, the percentage of GSCs increased from 0.96% to 1.65%. With 128 instances, a *t*-test demonstrates that this is a significant difference ($P < 0.0001$), with a mean difference between the groups of −0.69 with a 95% confidence interval of this difference from −0.72 to −0.65. This change in the percentage of GSCs was due to the cell interaction with TMZ.

Validation of model predictions in a genetically engineered mouse model of GBM. We next validated the mathematical modelling predictions through use of a mouse model in which tumour-bearing mice received either the optimized or the suboptimal treatment schedule in a randomized manner (Fig. 5a). A replication-competent avian sarcoma-leukosis virus (RCAS) long terminal repeat with a splice acceptor/tumour virus A-based PDGF-driven mouse model was used in concert with a *Cdkn2a*$^{-/-}$ (also known as *Ink4a/Arf*) germline mutation, which produces rapid and uniform gliomas. Tumour formation before treatment was confirmed by bioluminescence imaging and changes were recorded 72 h after the last treatment dose (Fig. 5b). These images provide insights into tumour volume growth as the radiance is correlated with size. Radiance in both groups before treatment was similar ($P = 0.95$, unpaired *t*-test). The average bioluminescence signal after treatment was 34% of the baseline signal with the optimized schedule versus 105% with the suboptimal schedule ($P = 0.008$, unpaired *t*-test; Fig. 5c). The median survival of mice in the optimized versus suboptimal groups was 11.5 d versus 9.5 d (log-rank hazard ratio = 0.46, 95% confidence interval = 0.24–0.87, $P < 0.001$; Fig. 5d), therefore validating the model predictions that the optimized schedule leads to superior outcomes.

Optimization of the relative timing of chemotherapy and radiation administrations. When considering the mechanism of differential efficacy of the optimized versus suboptimal schedule, we noticed that the optimized schedule tended to have shorter time intervals between TMZ and radiation administrations compared with the suboptimal schedule. We therefore set out to investigate whether including a radiosensitization effect of TMZ might lead to the identification of improved schedules. Specifically, a survival improvement might be achieved through optimizing the time interval between TMZ and radiation administrations such that radiation is administered at the time of peak TMZ concentration. Thus, the current standard-of-care administration schedule could be used with the exception that a specific time interval between TMZ and radiation administration would be prescribed. In contrast to the previous optimal schedule, this strategy would be simple to translate to patients with GBM.

To test TMZ-induced radiosensitization, we used the same mouse genetic background as above and updated our computational model to include a TMZ concentration dependence to the radiation-induced cell kill (equation (7)). Under these conditions, we first conducted a computational study to identify the optimal and suboptimal time intervals between administration of TMZ and radiotherapy. We again implemented stochastic optimization through the use of a simulated annealing strategy, with the fractional volume change at 30 d after the start of therapy as the defined fitness for each schedule. This systematic method identified that the optimal time interval between the administration of the two therapies is 41 min when using mouse parameters. The 30d fractional volume change for the identified schedules is shown in Fig. 6a and the reduction in relative fitness achieved using the optimization technique is demonstrated in Fig. 6b. Our findings demonstrate that the optimal and suboptimal offsets between therapies have a strong influence on the overall outcome. The influence of the interval size is visualized in Fig. 6c, in which fractional volume change is shown with a range of offsets around the identified optimum. Using just one dose of radiation per day, a similar behaviour is shown between schedules with optimal and suboptimal offsets and the derived optimal and suboptimal schedules discussed above. We further conducted a sensitivity analysis demonstrating that the results were robust to changes in the value of the radiosensitization parameter (Supplementary Fig. 2). To further assess the cellular response in the first 30 d after treatment initiation, we also investigated the change in average age, the distance from the vessel and the percentage of GSCs (Supplementary Fig. 3).

To validate the predictions of our computational modelling of the time interval between TMZ and radiation treatment, we conducted a mouse trial in an *Cdkn2a*$^{wt/wt}$ background, with its extended survival and opportunity for increased treatment events. For this study, all mice received RT at the same time of day (2 Gy per day for 5 d),

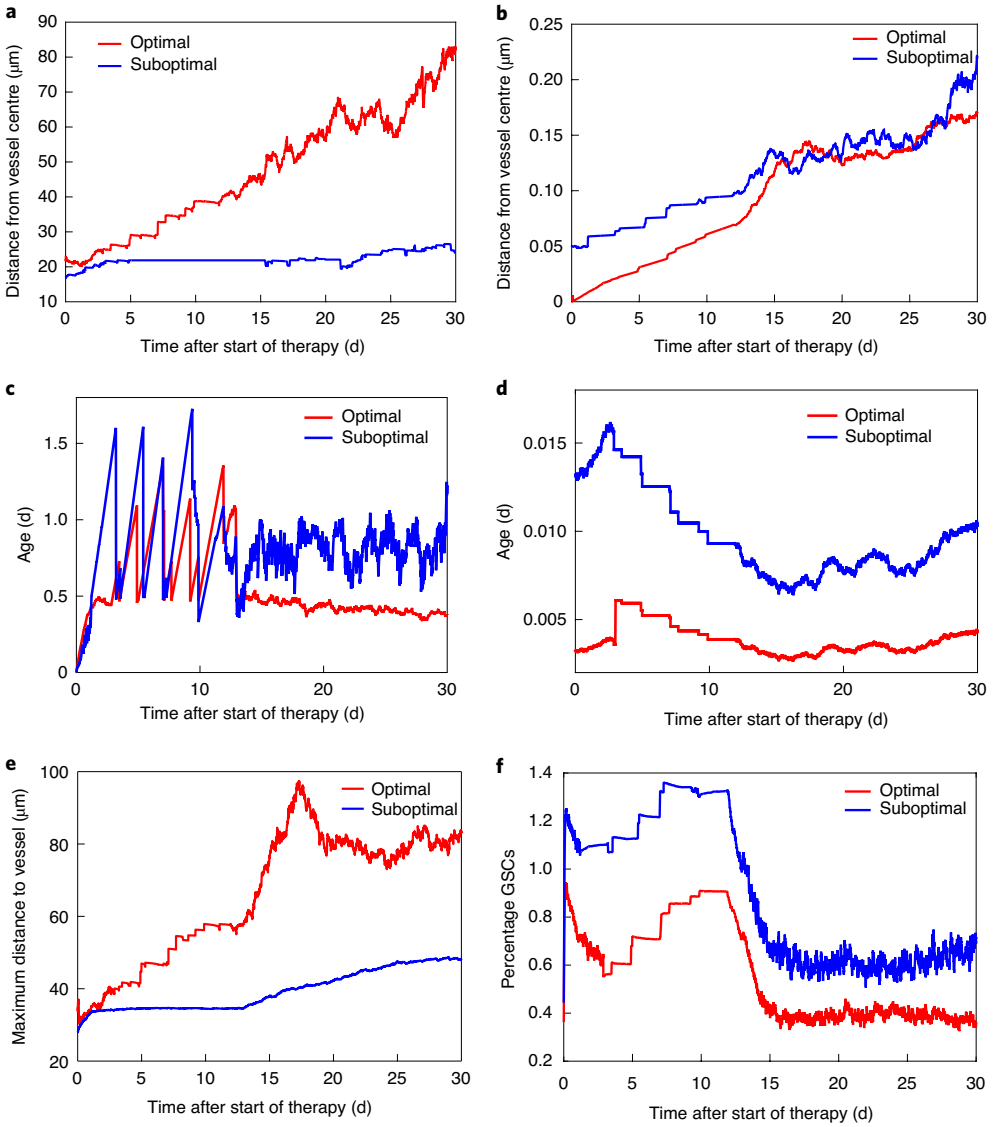

Fig. 4 | Prediction of GBM growth and treatment response. a,**b**, Prediction plots of the average distance of cells from the vessel centre up to 30 d after treatment commences for DTCs (**a**) and GSCs (**b**). **c**,**d**, The average age of the cells up to 30 d after the treatment started for DTCs (**c**) and GSCs (**d**). **e**, The maximum distance from the vessel that any of the cells travel up to 30 d after treatment commences. **f**, The percentage of cells that are GSCs up to 30 d after treatment initiation.

and the optimal group was administered TMZ 41 min before RT and the suboptimal group was administered TMZ 8 h after RT; the latter choice was made because TMZ is usually taken at bedtime by patients. The median survival of mice in this optimized versus suboptimal radiotherapy fractionation schedule was 34.5 d versus 30 d (log-rank hazard ratio = 0.3925, 95% confidence interval = 0.1613–0.9551, $P < 0.001$; Fig. 6d). The mouse study highlighted the importance of including radiosensitivity in the model considerations, as the survival time of the mice undergoing treatment with the optimized offset was slightly improved over the originally defined optimal schedule. Thus, the mouse trial validated our computational model predictions that the relative timing between TMZ and radiation adminstration plays an important role in determining survival.

The optimum schedule is robust when considering acquired resistance to chemoradiation. To assess the potential influence of the emergence of cells resistant to treatment due to the accumulation of (epi)genetic changes, we conducted a series of simulations with varying rates of appearance of resistant cells. Our model was modified to include a rate at which cells become resistant to chemoradiation, given by RR. Resistant cells were defined as cells that are impervious to both chemotherapy and radiotherapy. We then characterized the sensitivity of our results to the parameter RR. We varied its setting from 1×10^{-6} to 1×10^{-8} per cell division, as example rates at which resistance arises per cell division, and observed no significant change in the overall fractional volume change ($P = 0.7280$), percentage of GSCs ($P = 0.2921$) or the location of the cells ($P = 0.9743$; Supplementary Fig. 4). As we observed no significant change in the fractional volume change when resistance was introduced, no impact on the emergent optimized schedules is expected, as schedule fitness is defined on the basis of the size of the DTCs. As resistance to both chemotherapy and radiotherapy leads to no substantive change in population fitness, the weaker implementation, including a heterogeneous mix of radiotherapy-resistant and chemotherapy-resistant cells, has even less impact. Similarly, in this model, both GSCs and DTCs have the potential to generate resistant cells, providing a setup that would demonstrate maximal influence of the dynamics of emergence of resistant cells. As no

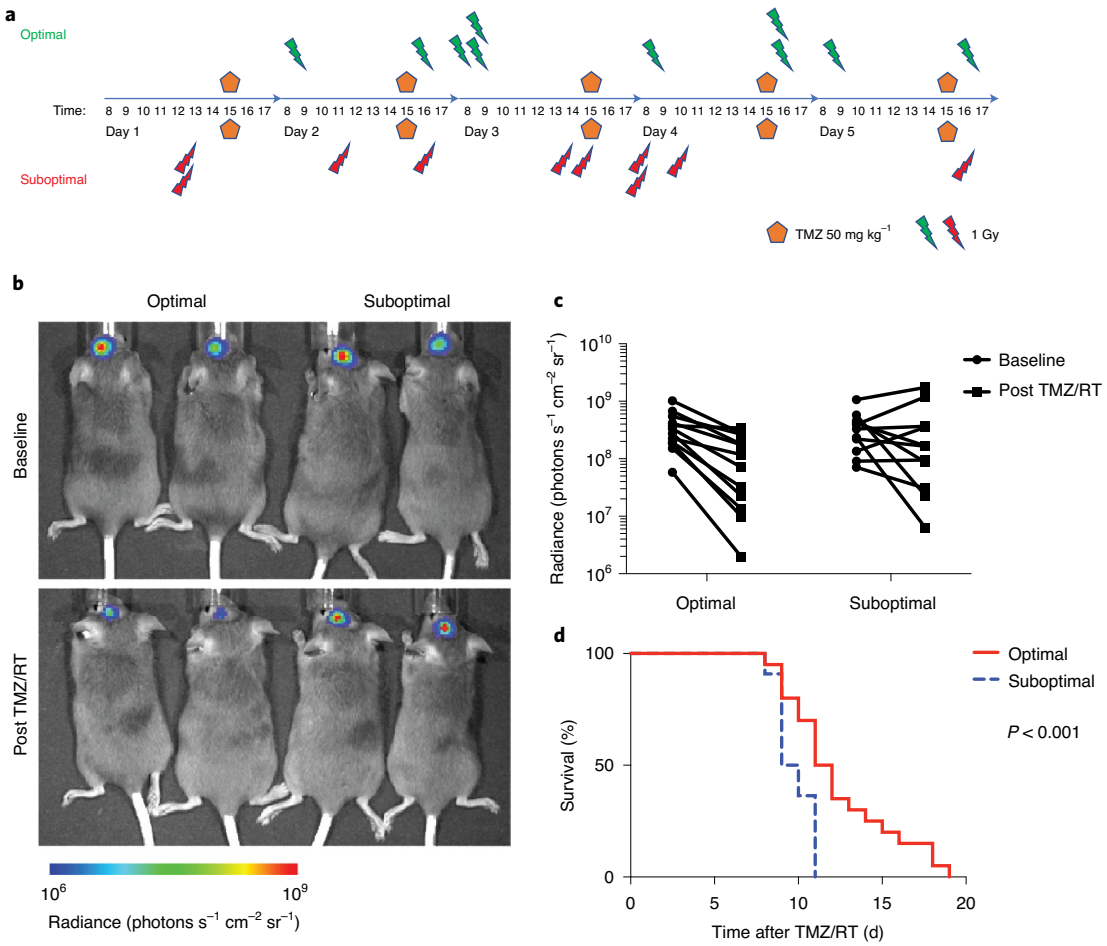

Fig. 5 | Validation of modelling predictions in a mouse model of GBM. a, Schematic of chemoradiation schedules applied to *N/t-va*; *Cdkn2a*$^{-/-}$; *Pten*$^{fl/fl}$; *Luc*$^{LSL/LSL}$:*Rcas-Pdgfb*; *cre* mouse GBMs. Optimal, optimized schedule; suboptimal, suboptimal schedule. The times indicate the hour according to the 24 h clock. **b**, Representative images of mice at the baseline and 72 h after treatment with the indicated chemoradiation schedules. Photographic images were overlain with a pseudocolour image to represent the spatial distribution of photon counts. Radiance in both groups before treatment was similar ($P = 0.95$, unpaired *t*-test). **c**, Quantification of radiance at the baseline and 72 h after the indicated treatments. Comparisons between the baseline and after combined chemoradiation with TMZ (TMZ/RT) were performed using a two-tailed unpaired *t*-test ($P = 0.95$) and an unpaired *t*-test ($P = 0.008$). **d**, Post-treatment survival of mice treated with the optimized schedule ($n = 20$) versus the suboptimal schedule ($n = 22$) ($n = 2$ chemoradiation schedules). The log-rank test was applied to compare the survival times (log-rank hazard ratio = 0.46, 95% confidence interval = 0.24–0.87, $P < 0.001$).

significant change was observed under these conditions, allowing only GSCs or DTCs to gain resistance results in an even smaller change. Here, the resistance rate RR was varied across two orders of magnitude and exhibited no measurable impact on the results; note that this finding might change if the rate is varied to a greater extent.

Translating the optimized administration schedule from mice to humans. When optimizing the schedules, we found that considering chemotherapy radiosensitization influenced the selection of the ideal offset between administration of chemotherapy and radiotherapy. All of the studies discussed above focused on mouse-derived pharmacokinetic (PK)/pharmacodynamic (PD) parameters. To understand how this research could be extrapolated to a future human study, we completed a large-scale computational study to identify the optimal offset under human-derived conditions. PK values were modified to match data for humans[19–21]. Under these conditions, the half-life of TMZ was set to 1.8 h, the dosage to 75 mg m^{-2}, T_{max} to 0.7 h and C_{max} to 3.7 mg l^{-1}. Treatment was undertaken for 6 weeks and we simulated 150 d from the start of therapy. We next used simulated annealing to identify the optimal offset, which we found to be 57 min. We then compared the identified optimal offset, the zero offset in which both therapies are administered about the same time and the schedule when radiation is administered at 15:00 but TMZ is given at bedtime, in this case 21:00. Table 1 presents the three assessed schedules: the derived optimum, the standard dosage of TMZ given at 15:00 and TMZ given at bedtime (21:00). Similar to the work described above for the mouse schedules, we used simulated annealing to identify the optimal schedule for human TMZ PK parameters. The fitness function was defined as the fractional volume change 150 d after the start of therapy. The optimization results are shown in Fig. 7a. The routine was initially seeded with the standard schedule and, during each generation, we randomly perturbed this schedule in 128 different ways that were simultaneously assessed. The schedule that produced the minimal fractional volume change was then used to seed the next generation. We found that the optimal schedule administered TMZ 57 min before radiation. The fractional volume change over the 150 d for each schedule is shown in Fig. 7b. We also assessed the distance from the vessel centre of both the DTCs (Fig. 7c) and GSCs (Fig. 7d). Finally, the percentage of the overall cell population comprising GSCs is shown in Fig. 7e. Thus, our model was able to predict schedules for potential testing in the clinic.

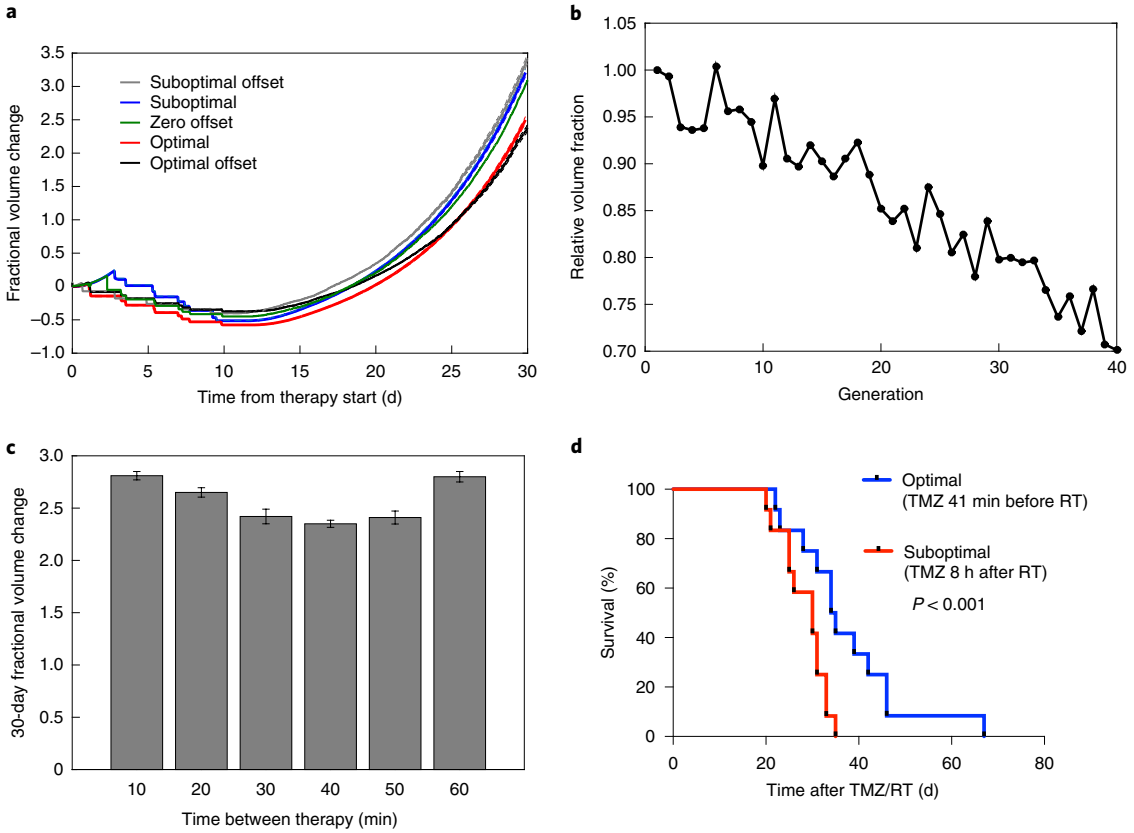

Fig. 6 | Identification of a combination schedule in mice by optimizing the offset between chemotherapy and radiotherapy. a, Prediction plots of the expected fractional volume change over time for the originally identified optimal and suboptimal schedules as well as schedules with the suboptimal and optimal offsets between therapy administrations. **b**, Relative fitness across stochastic optimization generations. Each generation consisted of 1,024 different schedules being tested with 128 instances of each schedule, creating the required technical replicates to account for model stochasticity. **c**, Fractional volume change under different offsets between radiotherapy and chemotherapy. Each schedule was simulated 50 times. Data are mean ± s.d. **d**, Survival of tumour-bearing mice (*N/t-va*; *Pten*$^{fl/fl}$:*Rcas-Pdgfb*; *cre* mouse GBMs) from after treatment with intraperitoneal TMZ and daily whole-brain irradiation with 2 Gy on 5 consecutive days (TMZ/RT). TMZ was administered 41 min before irradiation for the optimally treated mice ($n = 12$) and 8 h post-irradiation for the suboptimally treated mice ($n = 12$).

Discussion

Gliomas are cellularly and spatially complex, consisting of multiple cell types with differing proliferation rates and sensitivities to DNA damage-based standard-of-care therapy. Previously, we showed that there is interconversion between cell types in vivo during the time course of radiotherapy[22]. This insight led to the ability to optimize a schedule for radiotherapy alone, mirroring the clinical scenario of salvage radiotherapy for recurrent GBM, which achieved a substantial survival benefit[18] and is currently being tested in a clinical trial (NCT03557372). The various glioma cell types occupy specific locations within the tumours, with the least proliferative and treatment-responsive cells closest to the vessels. The standard-of-care therapy for newly diagnosed GBM is radiation, which delivers a uniform dose to all cells, and TMZ, which has time- and distance-dependent concentration gradients relative to the blood vessels, leading to a complex dynamic therapeutic response. To identify optimal treatment strategies, models are required that can capture this spatiotemporal complexity.

Here we developed a massively parallel computational model of the GBM microenvironment to systematically investigate the effects of different treatment schedules on outcomes. To investigate how specific parameters influence the success of chemoradiation therapy, we developed a technique to sample the search space using large-scale stochastic optimization. We conducted one of the largest simulation studies of tumour treatment response to date, using 36 million CPU hours on the Vulcan supercomputer. This enabled us to both examine the sensitivity of the treatment to TMZ pharmacokinetic and pharmacodynamic characteristics and study the relative efficacy of different administration schedules. Using this approach, we identified a chemoradiation schedule that was predicted to improve survival compared with standard schedules. This treatment strategy was then tested in a GBM mouse model and was found to indeed result in superior survival compared with the control schedule. Our approach is consistent with the hypothesis of spatial translocation of GSCs after cycling through a non-GSC state and the functional relevance of this process for resistance to chemoradiation.

When considering radiosensitivity, we identified that the survival outcome could be improved by optimally timing the distance between the administration of chemotherapy and radiotherapy. By timing the radiotherapy shortly after the administration of TMZ, there was enough time for the drug to diffuse to and interact with the cells. The optimal time between therapies was found to be shortly after the time at which the maximum concentration of TMZ is reached.

In summary, our computational approach identified that the close temporal association of TMZ treatment right before RT is paramount for improving the efficacy of this combination treatment. We reason that this temporal association of a synergistic effect of TMZ and RT may reflect not only the temporal restriction of the

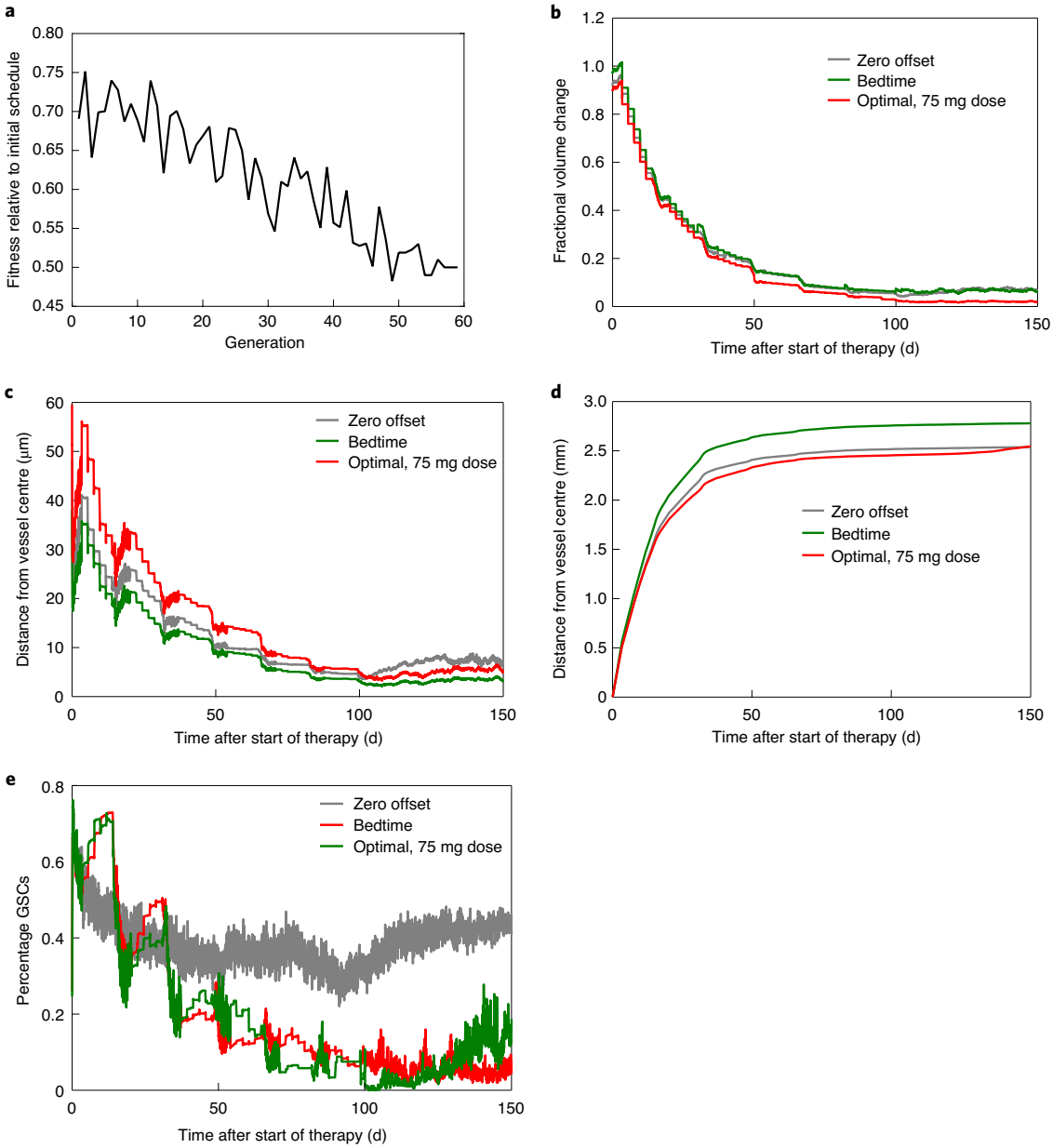

Fig. 7 | Identification of an optimum schedule for human validation. a, Relative volume fraction at each generation of the stochastic optimization routine. Each generation consisted of 1,024 different schedules being tested with 128 instances of each schedule, creating the required technical replicates to account for model stochasticity. **b**, The fractional volume change from baseline to 150 d after the start of therapy under the zero offset, bed and optimal low dose schedules. **c**,**d**, The average distance of cells from the centre of the vessel up to 150 d after treatment for DTCs (**c**) and GSCs (**d**). **e**, The percentage of overall cell population comprising GSCs up to 150 d after treatment commences.

interconversion of GSCs to a more chemosensitive state but also that this interconversion sets off early during the translocation of GSCs away from blood vessels, while they are still exposed to TMZ. Notably, using tissue markers to track GSCs in tissue has proven to be not feasible, probably because GSCs lose the expression of these markers after translocation away from the PVN.

Unfortunately, the necessary parameter values were not determined in one experiment by one laboratory for multiple individuals and there is therefore uncertainty connected to these values. Similarly, we did not have the ability to orthogonally validate all parameters. Furthermore, we considered that endothelial cells are constant over time, both in terms of number and spatial localization; therefore, changing blood vessels during angiogenesis are currently not considered in our research.

Our findings have clinically relevant implications for the treatment of patients with GBM. Phase-III randomized clinical trials demonstrating an important overall survival benefit from the addition of concurrent and adjuvant TMZ to radiation do not specify the time interval between TMZ and radiation administrations[23,24]. However, many oncologists administer TMZ at bedtime due to nausea[25]. This administration schedule is not supported by high-quality evidence regarding efficacy. The contribution of a synergistic interaction between radiation and TMZ to this improvement in survival is not known. However, a study of radiosensitization by TMZ in 20 different patient-derived orthotopic GBM xenografts showed that a subset of tumours exhibited synergy between radiation and TMZ when TMZ was administered 1 h before radiation[26]. Given that (1) a subset of patients could benefit from synergy between TMZ

and radiation; (2) no high quality evidence for the equivalence of bedtime administration of TMZ to administration shortly before radiotherapy exists; and (3) we have demonstrated in mice that administering TMZ shortly before radiotherapy improves overall survival compared with evening administration, we recommend that concurrent TMZ–radiotherapy for newly diagnosed GBM should use a 57 min interval between administration of TMZ and radiation. We believe that this time interval is driven by a combination of the time it takes for TMZ to reach its maximum concentration in a patient's bloodstream and the time it takes for TMZ to diffuse away from the blood vessel into the tumour and take its effect. As TMZ pharmacokinetics differ among patients and no data are available to investigate its variability within a population, we did not perform a sensitivity analysis to determine the range of time intervals that would be best for a patient population, but we expect that varying the optimum time by 5–10 min will lead to very similar results. As TMZ pharmacokinetics[19] predicts a rapid absorption but slow decay, we expect that earlier administration of TMZ relative to radiation (that is, a greater time interval than 57 min) will lead to smaller differences in outcome than later administration. A randomized clinical trial could be performed to directly test whether the administration time of TMZ affects overall survival.

However, the translation into clinical practice would need to take additional factors into account that affect therapeutic efficacy that might be present across a population of patients with GBM and within any one tumour. For example, the immune cell compartment, which comprises almost exclusively macrophages, was modelled only on the stroma functional level, because the interplay of macrophages and GSCs is widely elusive. In a rat glioma model, favourable modulation of the tumour-infiltrating lymphocyte composition by metronomic TMZ treatment schedules has been suggested[27], but translation of similar approaches to patients with GBM did not alter the outcome in the newly diagnosed[15] or recurrent setting[28], probably reflecting the overall lack of tumour-infiltrating lymphocytes in GBM[29]. Other variables that are not currently represented in these computational and mouse models that may or may not affect the optimal timing between TMZ and radiation include genetic alterations, such as subclonal mutations in p53 or the loss of PTEN[30–32], heterogeneity of expression patterns between[33] and within[34] tumours, and epigenetic heterogeneity[35]. Future studies will incorporate such heterogeneity as well as immunotherapy response modelling.

Methods

Generation of mouse GBMs. All animal experiments were approved by the Institutional Animal Care and Use Committee of the Fred Hutchinson Cancer Research Center (Protocol ID, 50842). Tumours were generated by injecting RCAS-transfected DF-1 cells into the brains of mice that express the t-va receptor under control of the nestin promoter (N/t-va). DF-1 cells were obtained from the American Type Culture Collection (ATCC, CRL-12203) and grown in Dulbecco's modified eagle medium containing 4 mM L-glutamine, 4.5 g l^{-1} glucose, 1 mM sodium pyruvate and 1.5 g l^{-1} sodium bicarbonate supplemented with 10% fetal bovine serum (DMEM, ATCC, 30-2002) at 39 °C without antibiotics. Transfections with custom-made RCAS-PDGFB-HA and RCAS-Cre were performed using the Fugene 6 transfection kit (Roche, 11814443001). Transfected cells (2×10^5) in 2 µl DMEM were injected into the brains of 6–8-week-old male or female *N/t-va*; *Cdkn2a*$^{-/-}$; *Pten*$^{fl/fl}$; *Luciferase*$^{LSL/LSL}$ or *N/t-va*; *Pten*$^{fl/fl}$ mice. The bodyweight of the mice used was 20–25 g. Mice were generated and bred in house, the genetic background was a mixture of 129/Sv, CJ7, C57BL6/J, FVB/N and BALB/C[36]. Hair at the site of surgery was removed using an off-the-shelf clipper. The coordinates from the bregma were as follows: lateral, 2 mm; anterior, 0.75 mm; depth, 2 mm. After developing symptoms such as lethargy, weight loss or pareses, mice were euthanized using carbon dioxide.

Mouse chemoradiotherapy. Mice were treated 3 weeks after tumour initiation with TMZ (LKT laboratories, 85622-93-1) 50 mg kg^{-1} body weight daily for 5 d concomitant to whole-brain irradiation with 2 Gy daily for 5 d. TMZ was freshly dissolved in phosphate-buffered saline with 0.5% dimethyl-sulfoxide before intraperitoneal injection. Irradiation to the head was performed under anaesthesia with isoflurane using the X-RAD 320 Biological Irradiator from Precision X-Ray. Mice were monitored to check for tumour-related symptoms, such as lethargy, weight loss (15% body weight), seizure, hyperactivity, altered gait, poor grooming, macrocephaly and paralysis. After developing symptoms, mice were euthanized using carbon dioxide.

Bioluminescence imaging. Tumour-bearing mice were anaesthetized with isoflurane and retro-orbitally injected with 75 mg kg^{-1} body weight D-luciferin (Caliper, 122796). Images were acquired 3 min after injection of luciferin for 5 s using the IVIS 100 imaging system (Caliper). A photographic image was overlain with the pseudocolour image to depict the spatial distribution of photon counts. A 1 cm^2 circular region centred manually between the ears was defined as a region of interest for the quantitation of radiance, defined as photons s^{-1} cm^{-2} sr^{-1}. Emission filters were set to 560–420 nm. No normalization or autofluorescence removal was performed. Mice were imaged before and 72 h after the last dose of treatment. Images of repeated measurements were set to the same scale. Hair removal was not performed before bioluminescence imaging, potentially limiting the accuracy of the in vivo imaging.

Anaesthesia. Isoflurane (Baxter, 1001936060) was used for anaesthesia during surgery for tumour generation, irradiation of the brain and bioluminescence imaging. A VetFlo vaporizer (Kent Scientific, VetFlo-1205S) was used, with a concentration of 5% in oxygen for induction and 2% in oxygen for maintenance of sedation.

Sample size for survival experiments. The sample size for survival experiments was calculated to detect a 10% increase in median survival with the optimal versus suboptimal chemoradiation schedules with 90% power at a 5% alpha level. Assumptions included a s.d. of survival of 10% for the first chemoradiation experiment, which was subsequently refined to 7.5%. Using an open resource sample size calculator (www.clincalc.com), these assumptions yielded sample sizes per arm of $n=20$ and $n=12$ mice, respectively.

Computational modelling. We designed a spatially explicit stochastic process model to investigate the impact of spatial localization on an evolving, heterogeneous tumour population. Inspired by the cell setup process established in CHASTE[37], we considered a 2D cross-section of the area surrounding a blood vessel (Fig. 2). For each proliferating cell type, we defined a stochastic cell cycle period t with a period defined as Uniform(t_{min}, t_{max}), after which the cell divides. For the initialization period before treatment, we enforce a shorter cell cycle to minimize the setup time without influencing the spatial locality or cell type. During the time of interest (during and after treatment), the range was set such to range from 0 h to 24 h, therefore having the cell divide typically once per day. To model cellular quiescence, we extended the time until cell division for the affected cell. To simulate a differentiation event, the cell dropped one level in the differentiation cascade. For GSCs, this event transformed the cell into a DTC at differentiation level $i=1$. For DTCs at differentiation level $i\neq z$, the cells remained classified as DTCs, but became more differentiated, gaining one level of differentiation. DTCs at level z became terminally differentiated cells. Regardless of cell type, the recently differentiated cells restarted their cell cycles. However, if the cells were quiescent, they maintained their quiescent period. Dedifferentiation events were treated in a similar manner: we considered a differentiation level $z_{revert}\leq z$ above which cells could dedifferentiate. DTCs at levels $1<i\leq z_{revert}$ became more stem-like, losing a differentiation level. DTCs at differentiation level $i=1$ became GSCs. Terminally differentiated cells and DTCs at differentiation levels $z_{revert}<i\leq z$ remained unaffected. Again, quiescence is also unaffected.

Spatial structure and interactions between cells. Each simulation was initialized with a blood vessel with a radius of d_{radius} cell radii and a single cell-thick layer of GSCs. The location of these endothelial cells was fixed throughout the simulation. Furthermore, a fraction p_{micro} of cells within a distance d_{micro} near the blood vessel are microenvironment cells, such as stromal cells. These microenvironment cells do not move or divide, but do provide constraints on cellular motion and can provide cell signalling[38]. Cells in the simulation each have a preferred cellular radius d and exert a force on other cells to ensure that cellular space. The cells naturally reside with their centres at a distance of two cell radii apart. The interaction stress between the cells is derived from the Lennard–Jones potential[39]. This stress was used to determine the force exerted on each cell and move the cells appropriately, therefore ensuring that no two cells were too close together. Glial cells are estimated to be roughly circular with a fixed radius of approximately 2 µm. This encapsulated the region that the glial cell and its appendages would occupy. Thus, in these 2D simulations, each cell was defined physically as a circular area with a fixed radius r and a cell's coordinates were defined on the basis of the cell centre. We centred the simulation on the blood vessel; as such, the cells comprising the blood vessel did not move. Microenvironmental cells were assumed to be fixed to an extracellular matrix and so are not pushed by other cells. Given the immobility of blood vessel and microenvironmental cells, all collision forces involving those cell types are propagated solely onto the colliding cell. We also assumed that GSCs were less motile than DTCs and were therefore less likely to move than the DTCs. Cells near the blood vessel are allowed to potentially change

their phenotypes at a probability that is proportional to the distance to the blood vessel to simulate the effects of microenvironment factors. Thus, only a fraction f_{STEM} of the total collision force was absorbed by stem cells while the remainder of the force affected DTCs. Collisions between cells of the same type distributed the force between the cells evenly.

Motion in this system was primarily the result of cell division. Cell division imposed forces between the resulting daughter cells. In stem cell niches, a gradient of soluble factors causes the spatial orientation of the offspring of stem cells[40]. Therefore, when a stem cell divided, the division occurred such that the more-differentiated daughter cell was oriented further away from the blood vessel, with a minimum separation distance imposed upon the cells. By contrast, non-stem divisions were randomly oriented. Once the division had occurred, normal collision resolution, as described above, was applied, separating the two daughter cells and propagating the motion to nearby cells. Although we did include a small term of random noise in the motion of cells, we did not consider high cellular motility and assumed that cells do not undergo high levels of either directed or undirected motion.

Radiotherapy. We considered the effects of radiotherapy to be independent of the spatial structure of the PVN—that is, the region of interest is small enough such that edge effects of radiation are not significant. As such, cell death in response to radiation was modelled by two probabilities: one probability for GSCs and one probability for DTCs. For type T, the probability of death from a single dose d of radiation was given by:

$$p_{T,\text{radio}}(d) = 1 - \exp\left(-\alpha_T \times d - \beta_T \times d^2\right) \quad (1)$$

following the well-known and used linear-quadratic model of radiation response[14]. We related the two radiation-based death terms by the following equalities: $\alpha_{GSC} = \rho \times \alpha_{TB}$ and $\beta_{GSC} = \rho \times \beta_{TB}$. Cells that did not die as a result of radiotherapy became quiescent for a type-dependent period of time—we modelled radiation-induced quiescence as an exponentially distributed increase in cell cycle length $Q_T \sim Q_{T,\min} + \text{exponential}(Q_{T,\text{mean}})$, where $Q_{T,\min}$ is the minimum quiescent period for type T and $Q_{T,\text{mean}}$ is the mean of the exponential distribution. Finally, radiotherapy is known to induce an increase in side population cells in gliomas[18]. As such, we considered a probability γ that a DTC undergoes a dedifferentiation event as described above.

TMZ. In contrast to the spatially uniform dose distribution of radiotherapy, the TMZ concentration is spatially heterogeneous and dependent on the spatial structure of the PVN. TMZ enters the tumour through absorption into the blood followed by diffusion into the PVN. Thus, we modelled a dose of TMZ as a combination of two functions. The blood concentration of TMZ, $C_{\text{blood}}(t)$, was modelled by exponential absorption of drug into the bloodstream until a maximum concentration $C_{\max}$ was reached, followed by an exponential decrease in drug concentration with half-life $t_{1/2}$:

$$C_{\text{blood}}(t) = \begin{cases} (\exp(rt) - 1)\, 2^{-\frac{t}{t_{1/2}}} & t < t_{\max} \\ C_{\max} 2^{-\frac{t - t_{\max}}{t_{1/2}}} & t \geq t_{\max} \end{cases} \quad (2)$$

where $r = \dfrac{\ln\left(\frac{C_{\max}}{2^{-\frac{t_{\max}}{t_{1/2}}}} + 1\right)}{t_{\max}}$

The parameter r in the above equation converts the known fixed point $(t_{\max}, C_{\max})$ into a rate of change of the drug concentration by solving the C_{blood} function. We based the functional form of the TMZ blood pharmacokinetic model on known pharmacokinetics of TMZ[16]. Diffusion of chemotherapeutic into the PVN was modelled by diffusion processes: we approximated the 2D diffusion partial differential equation:

$$\frac{\partial C}{\partial t} = D\left(\frac{\partial^2 C}{\partial x^2} + \frac{\partial^2 C}{\partial y^2}\right) \quad (3)$$

with the fundamental solution for the 2D diffusion equation given a single point source, positioned on the edge of the blood vessel:

$$C(t) = \frac{1}{4\pi D} \int_{\tau=0}^{\tau=t} \frac{1}{t-\tau} \exp\left(\frac{x^2 + y^2}{4D(t-\tau)}\right) \mathrm{d}\tau \quad (4)$$

As in the plasma, the TMZ degrades in the tumour. We assumed the half-life in tumour tissue to be similar to the half-life in the blood:

$$C(t) = \frac{1}{4\pi D} \int_{\tau=0}^{\tau=t} \frac{C}{t-\tau} \exp\left(\frac{x^2 + y^2}{4D(t-\tau)} - \frac{t-\tau}{t_{1/2}} \ln 2\right) \mathrm{d}\tau \quad (5)$$

To calculate the fraction of cells that die in a given time step at the given concentration, we set the EC_{50} value, the concentration at which the drug gives half-maximal response, for TMZ to 0.004268 mol m^{-3} on the basis of experiments by Wedge et al.[41] and calculated the EC_F value for the concentration using the following equation:

$$\text{EC}_F \left(\frac{F}{100 - F}\right)^{1/H} \text{EC}_{50} \quad (6)$$

where H is the Hill coefficient.

We set the Hill slope to 1.0 to represent a standard dose curve. We then stochastically determined whether a cell is killed due to chemotherapy in a given time step due to the response to the existing concentration of the chemotherapeutic that diffused to that cell's spatial location. Note that the values for determining diffusion and response to the dose level of TMZ are based on parameters estimated from data from mouse models[14]. To adjust the model to humans, these parameters should be adjusted to the values reported by Brock et al.[42].

Radiosensitization by TMZ. We considered the effects of a potential synergistic interaction between TMZ and radiation through the introduction of a radiosensitization parameter based on local TMZ concentration. The calculation of the probability of cell death from a single dose d of radiation (equation (1)) was modified to include a dependence on $C(t)$, the concentration of the chemotherapeutic at the time of radiation administration and k_{sens}, a constant representing the magnitude of the radiosensitization:

$$p_{T,\text{radio}}(d) = 1 - \exp(-\alpha_T \times (1 + k_{\text{sens}} \times C(t)) \times d - \beta_T \times d^2) \quad (7)$$

This modification to equation (1) enabled us to account for exposure to TMZ to make it more likely for a cell to die due to subsequent radiation. The likelihood of dedifferentiation or the time period of quiescence after radiation remained unchanged and modelled using the equations described above.

Parameter selection. Parameter estimates of cell cycle lengths for GSCs and non-stem-like cells were obtained from cell line experiments[18]. Estimation of z in GBMs is difficult; however, mouse experiments have determined the value $z = 5$ for normal brain glial cells[18]. The value of z_{revert} is unknown; we tested the effect of varying this parameter by conducting a sensitivity analysis. The number of DTCs started to vary significantly only when z_{revert} was less than 2 or greater than 14. We set z_{revert} to 7 for the subsequent simulations.

Using this simulation model, we investigated a set of cellular interactions and environmental effects characterized by GBM biology. We allowed cells near the blood vessel to revert to less differentiated states at a probability proportional to their distance to the blood vessel to simulate the effects of microenvironmental factors such as endothelial nitric oxide (eNOS)[38]. The diffusivity of eNOS has been experimentally determined[43]; however, the necessary concentration to induce a stem-like phenotype remains unknown. We initially imposed a linear decrease in the probability of reversion with decreasing concentration of eNOS. Furthermore, we allowed for an outward migration of cells similar to the motility of oligodendrocytic progenitor cells by imposing a force f_{move} to each cell oriented away from the blood vessel. A probability p_{death} of random cell death was also included and allowed to vary across differentiation levels. Therapeutic intervention was addressed as a change in the death dynamics of the system. During radiotherapy, cells undergoing proliferation are preferentially targeted; other cells die at much lower rates and instead halt their cell cycles for a period of time. By contrast, TMZ preferentially targets cells closest to the blood vessel since there the concentration of drug is largest; however, GSCs have lower rates of death compared with other cell types.

Schedule optimization and parallelization on a large-scale supercomputer. To derive optimized schedules, simulated annealing (SA)[44] was used. SA is a probabilistic algorithm that draws from statistical physics[45] and is used for a range of combinatorial optimization problems in which the goal is to identify, among many configurations, the one that minimizes a certain objective or fitness function; for example, the fitness function could be dependent on the total number of tumour cells over time such that the best schedule is the one that minimizes that number. The method starts with a template input and creates small perturbations from this template. The fitness function is then calculated for the perturbed input. If the fitness for the perturbed input is greater than that for the template input, then the perturbed input will serve as the template in the next iteration. If the fitness is lower, stochasticity is introduced by accepting the perturbation over the template with a certain probability that is gated by a time-dependent parameter and the degree of fitness degradation. At a fixed probability, the method will get a 'kick' whereby a randomly generated topology perturbation will be introduced. We defined the fitness function for minimization as the number of DTCs.

We defined a parallel implementation of SA such that the search space could be maximized and the likelihood of staying in a local minimum reduced. The SA method was adapted to the problem of schedule optimization by starting with the standard of care set as the template schedule. Perturbations were then created that matched the constraints that are outlined above. For the parallel version, many different perturbations to the schedule were created for simultaneous testing. To address the stochasticity in the problem, 128 runs for each schedule were simultaneously modelled. The average fitness for each schedule was determined, which was used for comparison. This research was completed on the Vulcan

supercomputer, an IBM Blue Gene/Q system, at the Lawrence Livermore National Laboratory. To complete the necessary simulations, 36 million CPU hours (4,109 years) on 131,072 cores were used.

Reporting Summary. Further information on research design is available in the Nature Research Reporting Summary linked to this article.

Data availability

The main data supporting the results in this study are available within the paper and its Supplementary Information. The raw and analysed datasets generated during the study are too large to be publicly shared, yet they are available for research purposes from the corresponding authors on reasonable request.

Code availability

The custom code used in this study is available at GitHub (https://github.com/arandles/chemoradiation) under the BSD-3-Clause open-source license.

Received: 17 April 2018; Accepted: 4 March 2021;
Published online: 16 April 2021

References

1. Weller, M. et al. EANO guidelines on the diagnosis and treatment of diffuse gliomas of adulthood. *Nat. Rev. Clin. Oncol.* **18**, 170–186 (2021).
2. Gramatzki, D. Glioblastoma in the Canton of Zurich, Switzerland revisited: 2005 to 2009. *Cancer* **122**, 3740–3741 (2016).
3. Ostrom, Q. T. et al. CBTRUS Statistical Report: primary brain and other central nervous system tumors diagnosed in the United States in 2013–2017. *Neuro Oncol.* **22**, iv1–iv96 (2020).
4. Khan, L. et al. External beam radiation dose escalation for high grade glioma. *Cochrane Database Syst. Rev.* CD011475 https://doi.org/10.1002/14651858.CD011475.pub2 (2016).
5. Louis, D. N. The 2016 World Health Organization classification of tumors of the central nervous system: a summary. *Acta Neuropathol.* **131**, 803–820 (2016).
6. Calabrese, C. et al. A perivascular niche for brain tumour stem cells. *Cancer Cell* **11**, 69–82 (2007).
7. Eyler, C. E. et al. Glioma stem cell proliferation and tumour growth are promoted by nitric oxide synthase-2. *Cell* **146**, 53–66 (2011).
8. Charles, N. et al. Perivascular nitric oxide activates notch signaling and promotes stem-like character in PDGF-induced glioma cells. *Cell Stem Cell* **6**, 141–152 (2010).
9. Bleau, A.-M. et al. PTEN/PI3K/Akt pathway regulates the side population phenotype and ABCG2 activity in glioma tumour stem-like cells. *Cell Stem Cell* **4**, 226–235 (2009).
10. Kozin, S. V., Duda, D. G., Munn, L. L. & Jain, R. K. Neovascularization after irradiation: what is the source of newly formed vessels in recurring tumors? *J. Natl Cancer Inst.* **104**, 899–905 (2012).
11. Garcia-Barros, M. et al. Tumor response to radiotherapy regulated by endothelial cell apoptosis. *Science* **300**, 1155–1159 (2003).
12. Radbruch, A. et al. Quantification of tumour vessels in glioblastoma patients using time-of-flight angiography at 7 Tesla: a feasibility study. *PLoS ONE* **9**, e110727 (2014).
13. Mustafa, D. et al. Expression sites of colligin 2 in glioma blood vessels. *Brain Pathol.* **20**, 50–65 (2010).
14. Houghton, P. J. et al. Antitumor activity of temozolomide combined with irinotecan is partly independent of O^6-methylguanine-DNA methyltransferase and mismatch repair phenotypes in xenograft models. *Clin. Cancer Res.* **6**, 4110–4118 (2000).
15. Gilbert, M. R. et al. Dose-dense temozolomide for newly diagnosed glioblastoma: a randomized phase III clinical trial. *J. Clin. Oncol.* **31**, 4085–4091 (2013).
16. Brada, M. et al. Temozolomide versus procarbazine, lomustine, and vincristine in recurrent high-grade glioma. *J. Clin. Oncol.* **28**, 4601–4608 (2010).
17. Minchinton, A. I. & Tannock, I. F. Drug penetration in solid tumours. *Nat. Rev. Cancer* **6**, 583–592 (2006).
18. Leder, K. Mathematical modelling of PDGF-driven glioblastoma reveals optimized radiation dosing schedules. *Cell* **7**, 603–616 (2014).
19. Stevens, M. F. et al. Antitumor activity and pharmacokinetics in mice of 8-carbamoyl-3-methyl-imidazo[5,1-*d*]−1,2,3,5-tetrazin-4(3*H*)-one (CCRG 81045; M & B 39831), a novel drug with potential as an alternative to dacarbazine. *Cancer Res.* **47**, 5846–5852 (1987).
20. Newlands, E. S. et al. Phase I trial of temozolomide (CCRG 81045: M&B 39831: NSC 362856). *Br. J. Cancer* **65**, 287–291 (1992).
21. Ostermann, S. et al. Plasma and cerebrospinal fluid population pharmacokinetics of temozolomide in malignant glioma patients. *Clin. Cancer Res.* **10**, 3728–3736 (2004).
22. Charles, N. A. & Holland, E. C. TRRAP and the maintenance of stemness in gliomas. *Cell Stem Cell* **6**, 6–7 (2010).
23. Stupp, R. et al. Radiotherapy plus concomitant and adjuvant temozolomide for glioblastoma. *N. Engl. J. Med.* **352**, 987–996 (2005).
24. Perry, J. R. et al. Short-course radiation plus temozolomide in elderly patients with glioblastoma. *N. Engl. J. Med.* **376**, 1027–1037 (2017).
25. Agarwala, S. S. & Kirkwood, J. M. Temozolomide, a novel alkylating agent with activity in the central nervous system, may improve the treatment of advanced metastatic melanoma. *Oncologist* **5**, 144–151 (2000).
26. Carlson, B. L. et al. Radiosensitizing effects of temozolomide observed in vivo only in a subset of O^6-methylguanine-DNA methyltransferase methylated glioblastoma multiforme xenografts. *Int. J. Radiat. Oncol. Biol. Phys.* **75**, 212–219 (2009).
27. Banissi, C., Ghiringhelli, F., Chen, L. & Carpentier, A. F. Treg depletion with a low-dose metronomic temozolomide regimen in a rat glioma model. *Cancer Immunol. Immunother.* **58**, 1627–1634 (2009).
28. Weller, M. et al. MGMT promoter methylation is a strong prognostic biomarker for benefit from dose-intensified temozolomide rechallenge in progressive glioblastoma: the DIRECTOR trial. *Clin. Cancer Res.* **21**, 2057–2064 (2015).
29. Thorsson, V. et al. The immune landscape of cancer. *Immunity* **48**, 812–830 (2018).
30. Wang, J. et al. Clonal evolution of glioblastoma under therapy. *Nat. Genet.* **48**, 768–776 (2016).
31. Snuderl, M. et al. Mosaic amplification of multiple receptor tyrosine kinase genes in glioblastoma. *Cancer Cell* **20**, 810–817 (2011).
32. Körber, V. et al. Evolutionary trajectories of IDHWT glioblastomas reveal a common path of early tumorigenesis instigated years ahead of initial diagnosis. *Cancer Cell* **35**, 692–704 (2019).
33. Wang, Q. et al. Tumor evolution of glioma-intrinsic gene expression subtypes associates with immunological changes in the microenvironment. *Cancer Cell* **32**, 42–56 (2017).
34. Patel, A. P. et al. Single-cell RNA-seq highlights intratumoral heterogeneity in primary glioblastoma. *Science* **344**, 1396–1401 (2014).
35. Capper, D. et al. DNA methylation-based classification of central nervous system tumours. *Nature* **555**, 469–474 (2018).
36. Hu, X. et al. mTOR promotes survival and astrocytic characteristics induced by Pten/AKT signaling in glioblastoma. *Neoplasia* **7**, 356–368 (2005).
37. Mirams, G. R. et al. Chaste: an open source C++ library for computational physiology and biology. *PLoS Comput. Biol.* **9**, e1002970 (2013).
38. Charles, N. & Holland, E. C. The perivascular niche microenvironment in brain tumour progression. *Cell Cycle* **9**, 3012–3021 (2010).
39. Verlet, L. Computer 'experiments' on classical fluids. I. Thermodynamical properties of Lennard-Jones molecules. *Phys. Rev.* **159**, 98–103 (1967).
40. Fuchs, E., Tumbar, T. & Guasch, G. Socializing with the neighbors: stem cells and their niche. *Cell* **116**, 769–778 (2004).
41. Wedge, S. R., Porteous, J. K., Glaser, M. G., Marcus, K. & Newlands, E. S. In vitro evaluation of temozolomide combined with X-irradiation. *Anticancer Drugs* **8**, 92–97 (1997).
42. Brock, C. S. et al. Phase I trial of temozolomide using an extended continuous oral schedule. *Cancer Res.* **58**, 4363–4367 (1998).
43. Thomas, V., Kumari, T. V. & Jayabalan, M. In vitro studies on the effect of physical cross-linking on the biological performance of aliphatic poly(urethane urea) for blood contact applications. *Biomacromolecules* **2**, 588–596 (2001).
44. Kirkpatrick, S., Gelatt, C. D. & Vecchi, M. P. Optimization by simulated annealing. *Science* **220**, 671–680 (1983).
45. Aarts, E. & Korst, J. *Simulated Annealing and Boltzmann Machines: A Stochastic Approach to Combinatorial Optimization and Neural Computing*. (John Wiley & Sons, 1989).

Acknowledgements

We acknowledge feedback and advice from members of the Michor laboratory, and D. Puleri for figure editing. We also acknowledge support from the Dana-Farber Physical Sciences Oncology Center (NIH U54CA193461, to F.M. and E.C.H.), the NIH Office of the Director (NIH, DP5OD019876, to A.R.), and the Lawrence Livermore National Laboratory Lawrence Fellowship (to A.R.). The mouse work was supported by P30 CA015704 at the Fred Hutchinson Cancer Research Center. This work was performed under the auspices of the US Department of Energy by Lawrence Livermore National Laboratory under Contract DE-AC52-07NA27344. Computing support for this work was provided by the Lawrence Livermore National Laboratory Institutional Computing Grand Challenges. F.M. acknowledges support from the Ludwig Center at Harvard.

Author contributions

A.R., H.-G.W., E.C.H. and F.M. contributed to the design of the study. A.R., J.A.D. and Y.-K.C. performed the computational modelling. H.-G.W., S.E. and S.S.P. performed the mouse experiments. E.C.H. and F.M. supervised the study. All of the authors contributed to the writing of the paper.

Competing interests
The authors declare no competing interests.

Additional information
Supplementary information The online version contains supplementary material available at https://doi.org/10.1038/s41551-021-00710-3.

Correspondence and requests for materials should be addressed to E.C.H. or F.M.

nature research

Corresponding author(s): Eric C. Holland and Franziska Michor

Last updated by author(s): Mar 4, 2021

Reporting Summary

Nature Research wishes to improve the reproducibility of the work that we publish. This form provides structure for consistency and transparency in reporting. For further information on Nature Research policies, see our Editorial Policies and the Editorial Policy Checklist.

Statistics

For all statistical analyses, confirm that the following items are present in the figure legend, table legend, main text, or Methods section.

n/a	Confirmed	
☐	☒	The exact sample size (*n*) for each experimental group/condition, given as a discrete number and unit of measurement
☐	☒	A statement on whether measurements were taken from distinct samples or whether the same sample was measured repeatedly
☐	☒	The statistical test(s) used AND whether they are one- or two-sided *Only common tests should be described solely by name; describe more complex techniques in the Methods section.*
☒	☐	A description of all covariates tested
☐	☒	A description of any assumptions or corrections, such as tests of normality and adjustment for multiple comparisons
☐	☒	A full description of the statistical parameters including central tendency (e.g. means) or other basic estimates (e.g. regression coefficient) AND variation (e.g. standard deviation) or associated estimates of uncertainty (e.g. confidence intervals)
☐	☒	For null hypothesis testing, the test statistic (e.g. *F*, *t*, *r*) with confidence intervals, effect sizes, degrees of freedom and *P* value noted *Give P values as exact values whenever suitable.*
☒	☐	For Bayesian analysis, information on the choice of priors and Markov chain Monte Carlo settings
☒	☐	For hierarchical and complex designs, identification of the appropriate level for tests and full reporting of outcomes
☒	☐	Estimates of effect sizes (e.g. Cohen's *d*, Pearson's *r*), indicating how they were calculated

Our web collection on statistics for biologists contains articles on many of the points above.

Software and code

Policy information about availability of computer code

Data collection	Data were collected using a software package that was made open-source under the BSD-3-Clause license. Custom code was used to generate the simulation data. This was written in C using the MPI library for parallelization. The code is available at https://github.com/arandles/chemoradiation.
Data analysis	Matlab R2015a was used to plot the results and Visit 2.10.0 was used to visualize cell locations.

For manuscripts utilizing custom algorithms or software that are central to the research but not yet described in published literature, software must be made available to editors and reviewers. We strongly encourage code deposition in a community repository (e.g. GitHub). See the Nature Research guidelines for submitting code & software for further information.

Data

Policy information about availability of data

All manuscripts must include a data availability statement. This statement should provide the following information, where applicable:

- Accession codes, unique identifiers, or web links for publicly available datasets
- A list of figures that have associated raw data
- A description of any restrictions on data availability

The main data supporting the results in this study are available within the paper and its Supplementary Information. The raw and analysed datasets generated during the study are too large to be publicly shared, yet they are available for research purposes from the corresponding authors on reasonable request.

Field-specific reporting

Please select the one below that is the best fit for your research. If you are not sure, read the appropriate sections before making your selection.

☒ Life sciences ☐ Behavioural & social sciences ☐ Ecological, evolutionary & environmental sciences

For a reference copy of the document with all sections, see nature.com/documents/nr-reporting-summary-flat.pdf

Life sciences study design

All studies must disclose on these points even when the disclosure is negative.

Sample size	No sample-size calculation was done for the mouse-survival experiment. On the basis of survival variability data from previous experiments using the same glioblastoma model, a minimum of 10 animals per treatment arm was deemed necessary to detect any relevant survival differences. We used a pooled analysis of replicates.
Data exclusions	No data were excluded from the analyses.
Replication	The survival experiment was repeated once, with similar results.
Randomization	Mice were numbered consecutively using ear tags. Mice with even numbers received the optimal irradiation schedule, and mice with uneven numbers received the suboptimal irradiation schedule, thereby stratifying age, gender and earlier-versus-later tumor initiation on the day of RCAS-based gene transfer.
Blinding	The laboratory technician assessing symptom-free survival was blinded to the applied irradiation schedule.

Reporting for specific materials, systems and methods

We require information from authors about some types of materials, experimental systems and methods used in many studies. Here, indicate whether each material, system or method listed is relevant to your study. If you are not sure if a list item applies to your research, read the appropriate section before selecting a response.

Materials & experimental systems

n/a	Involved in the study
☒	☐ Antibodies
☒	☐ Eukaryotic cell lines
☒	☐ Palaeontology and archaeology
☐	☒ Animals and other organisms
☒	☐ Human research participants
☒	☐ Clinical data
☒	☐ Dual use research of concern

Methods

n/a	Involved in the study
☒	☐ ChIP-seq
☒	☐ Flow cytometry
☒	☐ MRI-based neuroimaging

Animals and other organisms

Policy information about studies involving animals; ARRIVE guidelines recommended for reporting animal research

Laboratory animals	mus musculus, strain: N/tv-a;Ink4a/Arf-/-;PTENfl/fl;LucLSL/LSL 4-6 weeks of age, male or female
Wild animals	The study did not involve wild animals.
Field-collected samples	The study did not involve samples collected from the field.
Ethics oversight	All animal experiments were approved by the Institutional Animal Care and Use Committee of the Fred Hutchinson Cancer Research Center (protocol-ID 50842).

Note that full information on the approval of the study protocol must also be provided in the manuscript.